The Journal of Chemical Physics

Understanding size dependence of phase stability and band gap in $CsPbI_3$ perovskite nanocrystals

Ruo Xi Yang[1] and Liang Z. Tan[1, a)]
Molecular Foundry, Lawrence Berkeley National Lab

(Dated: 22 December 2019)

Inorganic halide perovskites $CsPbX_3$ (X = Cl, Br, I) have been widely studied as colloidal quantum dots for their excellent optoelectronic properties. Not only is the long-term stability of these materials improved via nanostructuring, their optical band gaps are also tunable by the nanocrystal size. However, theoretical understanding of the impact of nanocrystal size on the phase stability and band gap is still lacking. In this work, relative phase stability of $CsPbI_3$ as a function of the crystal size and chemical potential is investigated by density functional theory. The optically active phases (α- and γ-phase) are found to be thermodynamically stabilized against the yellow δ-phase by reducing the size of the NC below 5.6 nm in a CsI-rich environment. We developed a more accurate quantum confinement model to predict the change in band gaps at sub–10 nm regime by including finite-well effect. These predictions have important implications for synthesizing ever more stable perovskite NCs and band gap engineering.

I. INTRODUCTION

Lead halide perovskites have been at the centre stage of solar energy research as a promising photovoltaic material.[1,2] This class of materials possess favorable properties for optoelectronic applications, such as a tunable band gap, defect tolerance and high carrier mobility.[3] Despite the high power generation efficiency of halide perovskites achieved in the laboratory, their long-term performance is compromised by the structural instability and chemical volatility, which causes the prototype cubic crystal to break down under illumination, humidity and oxygen.[4–9] Among the hybrid organic-inorganic halide perovskites, $CN_3HN_3PbI_3$ readily dissociates into PbI_2 and CH_3NH_3I due to the volatility of the organic component.[10] While purely inorganic halide perovskites ($CsPbX_3$, X = halide)[11,12] have been proposed as a solution to the problem of methylammonium group chemical volatility[10], they present a different set of structural stability challenges. Upon prolonged storage, the optically active α-phase cubic $CsPbI_3$ transforms into the undesired yellow phase (δ-phase) at room temperature, due to the low formation energy of the δ-phase at room temperature and the high flexibility of the perovskite lattice.[13,14]

Varied approaches have been taken to stabilize the optically active phases of $CsPbI_3$, with nanostructuring[11,12,15], chemical doping[16], and strain engineering[17,18] emerging as viable strategies. Colloidal nanocrystal (NC) synthesis in particular is attractive because of the excellent optoelectronic properties of NCs, including high quantum yields, narrow emission widths, and tunable band gaps over the IR-UV range via halide composition engineering and quantum confinement effects.[19–21] In addition to their tunability, NC perovskites also exhibit enhanced phase stability compared to their bulk counterparts as the NC size decreases.[11,12,22] For example, while bulk α-$CsPbI_3$ can only be stablized at temperatures greater than 600 K, its NCs can be synthesized at room temperature.[11,12,19] Similar trends with NC size have also been observed in materials classes other than halide perovskites, such as metal nanocrystals and ferroelectric $BaTiO_3$.[23–25] In general, nanostructuring is thought to favor lower-density phases due to weaker cohesive forces than in the bulk.[26]

In this work, we present an ab-initio analysis of the phase diagram of $CsPbI_3$ nanocrystals as a function of nanocrystal size and synthesis conditions, showing that thermodynamic considerations stabilize the phase sequence of α- , γ- , δ-$CsPbI_3$ with increasing nanocrystal size. Furthermore, CsI-rich environments stabilize the optically active phases over the inactive δ phase. We consider associated changes in optical band gaps, developing an accurate quantum confinement model to predict band gap scaling with nanocrystal size, improving upon current models which fail for small NC sizes. Instead, our improved model includes finite-well effects, which accounts for wavefunction leakage beyond NC surfaces. As NC size is used to tune the optical properties for quantum dots, our model serves a more precise prediction in device design.

II. METHODS

We used density functional theory (DFT) as implemented in the Vienna ab initio simulation package (VASP).[27,28] The projector augmented-wave (PAW) method was used to describe the electron–core interaction.[29,30] The GGA functional PBEsol was used as the exchange-correlation functional in the structural relaxations and calculations of total energy.[31,32] A kinetic energy cutoff of 800 eV and 600 eV were used for the bulk and the surface, respectively. A Monkhorst–Pack mesh of $8 \times 8 \times 8$ k-point was used for the bulk α-phase, $6 \times 6 \times 6$ for bulk γ-phase, and $5 \times 5 \times 5$ for the δ-phase, where the k-point density is at least 0.04 Å. For slab calculations, the k-point mesh is set to $5 \times 5 \times 1$, $5 \times 5 \times 1$ and $4 \times 4 \times 1$ for α-phase, γ-phase and δ-phase, respectively. Only one k-point is considered along the c direction (with vacuum). Spin-orbital coupling (SOC) is not considered in the calculation of formation energies, since for the same compound it does not change the relative energy between phases.

a)Electronic mail: lztan@lbl.gov

FIG. 1. The crystal structure of the relaxed slabs from three perovskite phases along the c axis. The vacuum region (both sides) are cropped for visualization. Atoms outside the unit cell within $a-b$ plane are included to display the octahedra structure.

	Lattice constants (Å)	Number of octahedral layers
α-phase	a = 6.25	5
γ-phase	a = 8.37, b=8.95	8
δ-phase	a = 10.42, b=4.76	3

TABLE I. Lattice constants used in surface calculations

III. RESULTS AND DISCUSSION

Phase stability: First we computed the formation energies of three phases of cesium lead iodide ($CsPbI_3$) which are of most relevance: the cubic $Pm\bar{3}m$ phase referred to as α-phase, the orthorhombic *Pnma* perovskite phase referred to as γ-phase, and the orthorhombic yellow phase refered to as δ-phase (Fig.1). The formation energy is defined as $E_\mathrm{f} = E_{\mathrm{CsPbI_3}} - E_{\mathrm{CsI}} - E_{\mathrm{PbI_2}}$, where $E_{\mathrm{CsPbI_3}}$, E_{CsI} and $E_{\mathrm{PbI_2}}$ are the total enthalpies of the DFT calculations (Table II). Negative values indicate the bulk compound is stable against its constituent binaries. Positive formation energy of the α phase confirm its metastable nature, while γ- and δ-phase are thermodynamically stable. The results are consistent with the observations that, as temperature cools down, the polymorph transitions from α- to γ- and then to δ-phase.[13]

Since the bulk α phase is metastable, we suppose the surface energy plays a key role in stabilizing the structure at small crystal sizes. Therefore, we computed the surface energy for the three phases, each phase containing three Miller indexes: (100) (or (001)), (110), (111). For α- and γ-phase, each cut leaves two possible terminations: CsI-terminated slab or PBI_2-terminated slab. For δ-phase, the cleaved surface can be unambiguously chosen to not intersect PbI_6 octahedral units. For each slab configuration, we vary the layer of the slabs until it is well converged. For α-phase, the surface energy converged at 5 octahedral layers, for γ-phase, 8 layers and for δ-phase, 3 layers. Note that for γ-phase, more atomic layers are needed to achieve convergence. The vacuum is chosen to be at least 40 Å to ensure that the periodic images are placed far enough to minimize the interaction between themselves. We constructed the slab structure from the initial bulk symmetries and let the atomic positions to relax. The lattice constants along the a and b directions are fixed to their bulk value (Table I), i.e. only 1×1 unit cell is included in the lateral directions. Thus no further octahedral distortion is allowed by symmetry within the plane.

The surface energy is calculated by the equation[33]:

$$E_\mathrm{surf} = \frac{1}{2A}(E_\mathrm{slab} - N_b E_\mathrm{bulk} - \sum_i n_i\mu_i) \qquad (1)$$

where the E_slab is the DFT total energy of the slabs, A the surface area, E_bulk the DFT total energy of the bulk, N_b the number of formula unit the slab contains; μ_i is the chemical potential of the species at the surface termination, and n_i is the number of the species. Since for the α- and γ-phase the termination is not stoichiometric, E_surf depends on the chemical potential of the binary species. The chemical potential μ_i has to follow certain bounds[34]:

$$\mu_{\mathrm{CsI}} + \mu_{\mathrm{PbI_2}} = E_{\mathrm{CsPbI_3}}$$
$$\mu_{\mathrm{CsI}} \le E_{\mathrm{CsI}}$$
$$\mu_{\mathrm{PbI_2}} \le E_{\mathrm{PbI_2}}$$

These bounds ensure that the bulk does not decompose into the binaries. It is obvious that only one μ_i is an independent variable. For example, $\mu_{\mathrm{CsI}} = E_{\mathrm{CsI}}$ corresponds to a CsI-rich environment where the surface is in equilibrium to the bulk CsI, while $\mu_{CsI} = E_{\mathrm{CsPbI_3}} - E_{\mathrm{PbI_2}} = E_f + E_{\mathrm{CsI}}$ corresponds to a PbI_2-rich environment.

Assuming CsI surface is grown in CsI-rich condition and vice versa, for all α and γ symmetries, the lowest surface energy corresponds to the (100) facet with CsI termination (SI), as this termination breaks the least bonds and leaves minimal dangling bonds. For δ-phase, the surface is stoichiometric, thereby not affected by the chemical potential.

	α-phase	γ-phase	δ-phase
E_f (meV/f.m.u)	54.2	-85	-161
E_surf (meV/Å^2)	1.2	4.0	7.5

TABLE II. Formation energies of the bulk and surface energies for three perovskites phases calculated for CsI-rich environments.

As Table II shows, the α-phase has the lowest surface energy: 1.2 meV/Å^2, which corresponds to a 46.8 meV energy cost to form an areal unit cell in a surface. For γ-phase, the energy penalty is 299.7 meV per areal unit cell; for δ-phase 372.3 meV per areal unit cell. These differences are significant, and lead to NC size tunability of phase stability. In comparison, the surface energy of diamond is much higher at 5 J/m^2 (312 meV/Å^2).[35]

In the bulk, octahedral tilting of the PbI_6 cage breaks the symmetry of the cubic phase, and stabilizes the orthorhombic perovskite phase by reducing its energy. In contrast, the effects of octahedral rotation are less significant at surfaces than in the bulk, as evidenced by the small surface energies of the α-phase

With the computed surface energies, we can start to understand the NC size dependent phase stability. As the NC decreases in size, the surface/bulk ratio becomes larger, and the formation energy for the NC will differ significantly based on the surface energy. We approximate the total energy per formula unit of one NC to consist of two parts: the bulk part Δ_bulk and the surface part Δ_surf:

$$E_\mathrm{NC} = \Delta_\mathrm{bulk} + \Delta_\mathrm{surf} \qquad (2)$$

where the Δ_bulk equals the formation energy of the bulk E_f per formula unit, and

FIG. 2. Total energy of NC for three phases as a function of NC diameter.

$$\Delta_{\text{surf}} = \frac{E_{\text{surf}} \times 6d^2}{\frac{d^3}{V_0}} \tag{3}$$

where d is the diameter of the NC and V_0 the unit cell volume. As the perovskite quantum dots synthesized in experiments are cubes, for simplicity, we consider them to be isotropic in this model. Therefore, the surface area is $6d^2$, and the d^3/V_0 normalize the formula units. Then we have:

$$E_{\text{NC}} = E_{\text{f}} + \frac{6E_{\text{surf}} \times V_0}{d} \tag{4}$$

With Equation 3, we plot the relationship between E_{NC} and the NC size d for three different symmetries, as they possess varying E_f and E_{surf} (Fig.2). At the bulk limit, the total energy converges to the formation energies of the bulk ($\alpha > \gamma > \delta$), as the surface energy is negligible for large NCs. As the diameter decreases, the total energy starts to increase as surfaces cost energy to form. However, due to the differences in the surface energies, the total energies between phases start to compete at smaller diameters. Below $d = 5.6$ nm, the total energy of γ-phase NC is smaller than that of the yellow δ-phase, meaning that the γ-phase becomes thermodynamically more stable. Further reducing the size below 3.7 nm lets the cubic α-phase become energetically favorable to the yellow phase, and finally overtake the orthorhombic δ-phase below 2.7 nm.

These predictions are consistent with existing experiments, with phase-stable NCs of sizes typically ranging from 3 nm to 16 nm.[12,19,21,36] The discrepancies between our calculations and the experiments can come from two factors: finite-temperature effects and kinetic trapping during growth. Firstly, the vibrational entropy is expected to lower the free energy of the α and γ phase NCs more than the δ phase NCs, due to the less compact crystal structure of the former admitting larger dynamic disorder. This effect would tend to stabilize the α and γ phases at larger NC sizes. However, this effect is expected to be limited as only the differences in vibrational entropies of bulk and slab forms would appear in the calculation of surface free energies (equation (1)). Secondly, similar to the bulk perovskites, the NCs may experience kinetic barriers for the phase transitions during synthesis, where the optically active phases are "trapped" before degrading. The dependence of these kinetic effects on environmental conditions is likely to explain the variation of NC sizes in experiments.[37] The implication of these results is that the increase in stability of cubic and orthorhombic phases in NC form have an intrinsic origin in their favorable phase structure at NC surfaces, independent of effects such as passivation by ligands.

Depending on the stoichiometry, the surface energy is a function of the chemical potential of the constituent compounds, μ_{CsI} or μ_{PbI_2}. Additionally, the NC total energy is a function of the surface energy E_{surf} and the NC size d. We therefore consider a phase diagram with two variables μ_{CsI} and d that can be controlled in synthesis to achieve favorable NC phases. Fig.3 shows phase diagram as a function of both d and $\Delta\mu_{\text{CsI}}$, which represents the lowest total energy curve in Fig.2, with varying d and $\Delta\mu$. We have taken the upper bound of μ_{CsI} to be E_{CsI}, corresponding to CsI-rich condition; and the lower bound to be $E_{\text{CsPbI}_3} - E_{\text{PbI}_2}$, corresponding to CsI-poor. Here, E_{CsPbI_3} is the total energy of the bulk γ-phase. To achieve the the favourable perovskite phases, a combination of small d and large $\Delta\mu_{\text{CsI}}$ (CsI-rich environment) should be chosen.

Quantum confinement: Quantum confinement of electronic states results from the small length scale of nanoparticles, which usually range from 1 – 25 nm, changing the continuous band structure of a bulk semiconductor into discrete energy levels and increasing its band gap. In the most commonly used model, nanostructuring is modeled by a potential well for the carriers, increasing their quasiparticle energies and hence the band gap. The Schrödinger equation is written as:

$$[-\frac{\hbar^2}{2m}\nabla^2 + V(r)]\Psi = E\Psi \tag{5}$$

where the $V(r)$ is the height of the well. The simplest model assumes infinite potential wells, $V(r > d) = 0$ and $V(r < d) = -\infty$, and the boundary conditions that the wavefunction must go to zero outside the potential well. The solution is particularly simple:

$$E_n = \frac{\pi^2\hbar^2 n^2}{2m^* d^2}, n = 1, 2... \tag{6}$$

where the m^* is the effective mass for electrons/holes. Here we used $m_e^* = 0.18m_e$ and $m_h^* = 0.22m_e$, calculated using the PBE exchange-correlation functional with SOC.[38] The change in the band gap from its bulk value is given by the first allowed ($n = 1$) energy levels of the electrons and holes[39], yielding;

$$\Delta E_g = \frac{\pi^2\hbar^2}{2m_e^* d^2} + \frac{\pi^2\hbar^2}{2m_h^* d^2} \tag{7}$$

ΔE_g is plotted as a function of $1/d$ in Fig.5. At the bulk limit, the quantum confinement effect vanishes and the band gap converges to the bulk value. As NC size reduces, the quantum confinement effect becomes more pronounced, opening the band gap significantly. The monotonic trend matches well with experiments (Fig.5), the simple infinite well model drastically overestimates the value of the band gaps.

To address this mismatch, we considered a corrected model where the finite potential is taken into account. In this model, the potential well is not infinite, but is equal to the work function (ϕ) of the slabs: $V(r > d) = 0$ and $V(r < d) = -\phi$, thus changing the boundary conditions. ϕ is computed by the equation:

$$\phi = \varepsilon_{\text{fermi}} - VL \tag{8}$$

FIG. 3. Phase diagram of α-, γ- and the δ-phase, as a function of the chemical potential $\Delta\mu_{\mathrm{CsI}}$ and the NC size d. $\Delta\mu_{\mathrm{CsI}} = \mu_{\mathrm{CsI}} - E_{\mathrm{CsI}}$. The gradient infers the difference in total energy between α- and γ-phase (blue), and between γ- and δ-phase, respectively.

FIG. 4. Electrostatic potential of the slab of α-phase $CsPbI_3$ along the c direction (blue dashed line). Green dashed line represents the Fermi level E_F, and $V_{slab}^{interior}$ is the average local potential. V_{vac} and Φ denote the vacuum level and work function, respectively.

Thickness d (nm)	1.89	2.51	3.15
Work function ϕ (eV)	5.19	5.15	5.12
Energy shift ΔE (eV)	0.564	0.365	0.251

TABLE III. The lengths and height of the potential well, and the corresponding energy shift for the cubic α-phase perovskite.

where $\varepsilon_{\mathrm{fermi}}$ is the Fermi level of the electrons and VL the electrostatic potential at the vacuum, both calculated using PBEsol function (illustrated in Fig.4). The results for different slabs are summarized in Table III.

For the finite well, the wavefunction no longer vanishes to zero at the potential wall, but decays exponentially outside the wall. The ground state wavefunction depends self-consistently on the energy eigenvalue, which we solve for by numerical iteration:

$$\psi = Ae^{-\alpha r}, \text{where}\, \alpha = \sqrt{2m(\phi - E)/\hbar} \tag{9}$$

A calculation of ΔE at 1.89, 2.51 and 3.15 nm, with the work function of 5.19, 5.15 and 5.12 eV (the thickness of slabs in our DFT calculations), yields the results: 0.506, 0.321, and 0.219 eV, respectively (Table III). Using the constant work function value (5.12 eV) from the thickest slab in our DFT calculations with different quantum well sizes gives almost identical results, as plotted in Fig.5. This is to be expected as the potential well height is mostly constant over the NC size range. Using the constant work function (5.12 ev), we estimated the change in the band gap for larger NCs. The results can be fitted to $\Delta E_g = a/d^2$, where $a = 2.686$. The impact of the finite well is that it rectifies the overconfinement of the infinite well model, reducing the energy shift within the quantum well, and leading to a smaller band gap. The finite potential well model has also been appied to 2D layered perovskites[40], where it was shown that it performed better for thicker 2D perovskite layers due to the break down of the continuum approximation for the thinnest layers.

A further improvement to the model extends the one-dimensional finite quantum well to three dimensions. We take $V(r)$ to be a cube-shaped potential well of depth ϕ, and solve equation (5) in the planewave basis. The results of the 3D finite well model are shown in Fig.5, which lie between the 1D infinite- and finite-well models. While the infinite-well model over confines the wavefunctions, the finite-well model relaxes the confinement in 1D, leaving the carriers unconfined along other two dimensions, thereby results in an underestimation of the energy shift. The 3D potential well, however, corrects the error from both approximations and hence matches well with the experiments, particularly at larger crystal sizes. At NC sizes smaller than 7 nm, the 3D model starts to overestimate the band gap, likely due to the breakdown of the continuum approximation at these sizes.

For comparison, we have directly computed the band gaps of small slabs using DFT, with PBEsol and SCAN functionals. Since GGA and metaGGA are known to underestimate the band gap, the E_g directly calculated are smaller than that measured (1.08 eV for PBEsol and 1.24 eV for SCAN). Nevertheless, the change E_g between bulk and slab forms is still reliable. The DFT calculations also confirmed that the band gap increases as NC size reduces, and agrees well with our 1D model at larger slab sizes. As slab size reduces to sub-2 nm, the discrepancy between the model and DFT becomes larger, indicating a drastic change in the electronic structure, at which scale the confinement may no longer be considered a perturbation to the band structure, as the periodicity of the crystal is largely compromised at this size. Therefore, continuum models are likely to be poor approximations for the electronic structure of small NCs.

The remaining discrepancies between the theoretical predictions and the measured band gap arise from effects other than quantum confinement of free carriers. One possible source of error could be that the local symmetry in $CsPbI_3$ is dynamically broken, resulting in a larger band gap on average.[41–46] However, dynamical symmetry breaking is expected to be present in both bulk and NC forms. While excitons in halide perovskites have Bohr radii similar to the nanocrystal diameter, and exhibit measurable confinement effects[47], the exciton binding energies E_b in halide perovskites are typically less than 50 meV[48], and are small compared to the band gap changes due to the band energy quantum confinement effects described above. The exciton binding energy for $CsPbI_3$ is estimated to be 20 meV[11], smaller than the thermal energy k_BT. Evidence of the extent to which nanostructuring influences the exciton binding energy in halide perovskites is unclear, with varied values of E_b reported depending on the characterization method.[49,50]

FIG. 5. Band gap change as a function of NC size. The NC experiments are referenced from literature[12], where $\Delta E_g = E_{g,\mathrm{NC}} - E_{g,\mathrm{bulk}}$ (1.73 eV). The orange circles denote the calculated band gap shift from our finite-well model with individual quantum well size and work function from Table 4. The green circles use a single work function (5.12 eV) from the thickest slab with varying well sizes and is fitted to $1/d^2$ (green dashed line). The ΔE_g for PBEsol and SCAN functional is calculated by $\Delta E_g = E_{g,\mathrm{slab}} - E_{g,\mathrm{bulk}}$.

IV. CONCLUSION

Using DFT, we studied three competing phases of $CsPbI_3$ as a function of NC size and synthesis conditions, and solved for the conditions under which the optically active phases can be stabilized. The size dependence of the phase stability is shown to have an intrinsic origin in the surface structure of the perovskite phases. Our model for predicting the band gap changes with NC size improves upon current infinite-well models, providing better predictions for small NCs, and showing that the finite potential barrier at the NC surface is crucial for understanding the electronic structure of halide perovskite NCs. In summary, these predictions will enable improved control of the optically active halide perovskite phases via nanostructuring, and of their optoelectronic properties.

V. SUPPLEMENTARY MATERIALS

The supporting information is available via Supporting Information.

ACKNOWLEDGMENTS

We thank Aaron Fafarman for discussions that led to this work. RXY and LZT were supported by the Molecular Foundry at Lawrence Berkeley National Laboratory, supported by the Office of of Science, Office of Basic Energy Sciences, of the US Department of Energy, under contract No. DE-AC02-05CH11231. Computational support was provided by the NERSC of the U.S. Department of Energy.

[1] A. Kojima, K. Teshima, Y. Shirai, and T. Miyasaka, "Organometal Halide Perovskites as Visible-Light Sensitizers for Photovoltaic," J. Am. Chem. Soc. **131**, 6050–6051 (2009).

[2] M. M. Lee, J. Teuscher, T. Miyasaka, T. N. Murakami, and H. J. Snaith, "Efficient Hybrid Solar Cells Based on Meso-superstructured Organometal Halide Perovskites," Science **338**, 643–647 (2012).

[3] W. S. Yang, J. H. Noh, N. J. Jeon, Y. C. Kim, S. Ryu, J. Seo, and S. I. Seok, "High-performance photovoltaic perovskite layers fabricated through intramolecular exchange," Science **348**, 1234–1237 (2015).

[4] W. Nie, J.-C. Blancon, A. J. Neukirch, K. Appavoo, H. Tsai, M. Chhowalla, M. A. Alam, M. Y. Sfeir, C. Katan, J. Even, S. Tretiak, J. J. Crochet, G. Gupta, and A. D. Mohite, "Light-activated photocurrent degradation and self-healing in perovskite solar cells," Nature Communications **7** (2016).

[5] H. Yuan, E. Debroye, K. P. Janssen, H. Naiki, C. Steuwe, G. Lu, M. Moris, E. Orgiu, H. Uji-i, F. De Schryver, P. Samori, J. Hofkens, and M. B. Roeffaers, "Degradation of Methylammonium Lead Iodide Perovskite Structures through Light and Electron Beam Driven Ion Migration," J. Phys. Chem. Lett. , acs.jpclett.5b02828 (2016).

[6] Y. Li, X. Xu, C. Wang, B. Ecker, J. Yang, J. Huang, and Y. Gao, "Light-Induced Degradation of $CH_3NH_3PbI_3$ Hybrid Perovskite Thin Film," The Journal of Physical Chemistry C **121**, 3904–3910 (2017).

[7] Q. Wang, B. Chen, Y. Liu, Y. Deng, Y. Bai, Q. Dong, and J. Huang, "Scaling behavior of moisture-induced grain degradation in polycrystalline hybrid perovskite thin films," Energy Environ. Sci. **10**, 516–522 (2017).

[8] D. Bryant, N. Aristidou, S. Pont, I. Sanchez-Molina, T. Chotchunangatchaval, S. Wheeler, J. R. Durrant, and S. A. Haque, "Light and oxygen induced degradation limits the operational stability of methylammonium lead triiodide perovskite solar cells," Energy & Environmental Science **9**, 1655–1660 (2016).

[9] M.-G. Ju, M. Chen, Y. Zhou, J. Dai, L. Ma, N. P. Padture, and X. C. Zeng, "Toward Eco-friendly and Stable Perovskite Materials for Photovoltaics," Joule **2**, 1231–1241 (2018).

[10] D. P. Nenon, J. A. Christians, L. M. Wheeler, J. L. Blackburn, E. M. Sanehira, B. Dou, M. L. Olsen, K. Zhu, J. J. Berry, and J. M. Luther, "Structural and chemical evolution of methylammonium lead halide perovskites during thermal processing from solution," Energy & Environmental Science **9**, 2072–2082 (2016).

[11] L. Protesescu, S. Yakunin, M. I. Bodnarchuk, F. Krieg, R. Caputo, C. H. Hendon, R. X. Yang, A. Walsh, and M. V. Kovalenko, "Nanocrystals of Cesium Lead Halide Perovskites ($cspbi_3$, X = Cl, Br, and I): Novel Optoelectronic Materials Showing Bright Emission with Wide Color Gamut," Nano Lett. **15**, 3692–3696 (2015).

[12] A. Swarnkar, A. R. Marshall, E. M. Sanehira, B. D. Chernomordik, D. T. Moore, J. A. Christians, T. Chakrabarti, and J. M. Luther, "Quantum dot – induced phase stabilization of α-$CsPbI_3$ perovskite for high-efficiency photovoltaics," , 31–34 (2016).

[13] R. J. Sutton, M. R. Filip, A. A. Haghighirad, N. Sakai, B. Wenger, F. Giustino, and H. J. Snaith, "Cubic or Orthorhombic? Revealing the Crystal Structure of Metastable Black-Phase CsPbI3 by Theory and Experiment," ACS Energy Lett. **3**, 1787–1794 (2018).

[14] T. Wu, Y. Wang, Z. Dai, D. Cui, T. Wang, X. Meng, E. Bi, X. Yang, and L. Han, "Efficient and Stable $CsPbI_3$ Solar Cells via Regulating Lattice Distortion with Surface Organic Terminal Groups," Advanced Materials , 1900605 (2019).

[15] A. Marronnier, G. Roma, S. Boyer-Richard, L. Pedesseau, J.-M. Jancu, Y. Bonnassieux, C. Katan, C. C. Stoumpos, M. G. Kanatzidis, and J. Even, "Anharmonicity and Disorder in the Black Phases of Cesium Lead Iodide Used for Stable Inorganic Perovskite Solar Cells," ACS Nano **12**, 3477–3486 (2018).

[16] S. Dastidar, D. A. Egger, L. Z. Tan, S. B. Cromer, A. D. Dillon, S. Liu, L. Kronik, A. M. Rappe, and A. T. Fafarman, "High Chloride Doping Levels Stabilize the Perovskite Phase of Cesium Lead Iodide," Nano Letters **16**, 3563–3570 (2016).

[17] S. Ma, S. H. Kim, B. Jeong, H. Kwon, S. Yun, G. Jang, H. Yang, C. Park, D. Lee, and J. Moon, "Strain-Mediated Phase Stabilization: A New Strategy for Ultrastable $\alpha-CsPbI_3$ Perovskite by Nanoconfined Growth," Small **15**, 1900219 (2019).

[18]J. A. Steele, H. Jin, I. Dovgaliuk, R. F. Berger, T. Braeckevelt, H. Yuan, C. Martin, E. Solano, K. Lejaeghere, S. M. J. Rogge, C. Notebaert, W. Vandezande, K. P. F. Janssen, B. Goderis, E. Debroye, Y.-K. Wang, Y. Dong, D. Ma, M. Saidaminov, H. Tan, Z. Lu, V. Dyadkin, D. Chernyshov, V. Van Speybroeck, E. H. Sargent, J. Hofkens, and M. B. J. Roeffaers, "Thermal unequilibrium of strained black $CsPbI_3$ thin films," Science **365**, 679–684 (2019).

[19]A. Dutta, S. K. Dutta, S. DasAdhikari, and N. Pradhan, "Phase-Stable CsPbI3 Nanocrystals: The Reaction Temperature Matters," Angewandte Chemie International Edition **57**, 9083–9087 (2018).

[20]G. Nedelcu, L. Protesescu, S. Yakunin, M. I. Bodnarchuk, M. Grotevent, and M. V. Kovalenko, "Fast anion-exchange in highly luminescent nanocrystals of cesium lead halide perovskites (CsPbX3, X=Cl, Br, I)," Nano Lett. **15**, 5635–5640 (2015).

[21]F. Liu, Y. Zhang, C. Ding, S. Kobayashi, T. Izuishi, N. Nakazawa, T. Toyoda, T. Ohta, S. Hayase, T. Minemoto, K. Yoshino, S. Dai, and Q. Shen, "Highly Luminescent Phase-Stable CsPbI3 Perovskite Quantum Dots Achieving Near 100% Absolute Photoluminescence Quantum Yield," ACS Nano **11**, 10373–10383 (2017).

[22]X. Kong, K. Shayan, S. Hua, S. Strauf, and S. S. Lee, "Complete suppression of detrimental polymorph transitions in all-inorganic perovskites via nanoconfinement," ACS Applied Energy Materials **2**, 2948–2955 (2019), https://doi.org/10.1021/acsaem.9b00322.

[23]C. C. Yang and S. Li, "Size-Dependent Phase Stability of Silver Nanocrystals," The Journal of Physical Chemistry C **112**, 16400–16404 (2008).

[24]M. J. Mayo, A. Suresh, and W. D. Porter, "Thermodynamics for Nanosystems: Grain and Particle-size Dependent hase Diagrams," **5**, 100–109 (2003).

[25]S. Schlag and H.-F. Eicke, "Size driven phase transition in nanocrystalline $BaTiO_3$," Solid State Communications **91**, 883–887 (1994).

[26]P. Ayyub, V. R. Palkar, S. Chattopadhyay, and M. Multani, "Effect of crystal size reduction on lattice symmetry and cooperative properties," Physical Review B **51**, 6135–6138 (1995).

[27]G. Kresse and J. Furthmüller, "Efficient Iterative Schemes for Ab Initio Total-energy Calculations Using a Plane-wave Basis Set," Phys. Rev. B **54**, 11169–11186 (1996).

[28]G. Kresse and J. Furthmüller, "Efficient Iterative Schemes for Ab Initio Total-energy Calculations Using a Plane-wave Basis Set," Phys. Rev. B **54**, 11169–11186 (1996).

[29]P. E. Blöchl, "Projector Augmented-wave Method," Phys. Rev. B **50**, 17953–17979 (1994).

[30]G. Kresse and D. Joubert, "From ultrasoft pseudopotentials to the projector augmented-wave method," Phys. Rev. B **59**, 1758–1775 (1999).

[31]J. P. Perdew, A. Ruzsinszky, G. I. Csonka, O. A. Vydrov, G. E. Scuseria, L. A. Constantin, X. Zhou, and K. Burke, "Restoring the Density-Gradient Expansion for Exchange in Solids and Surfaces," Phys. Rev. Lett. **100**, 136406 (2008).

[32]J. P. Perdew, A. Ruzsinszky, G. I. Csonka, O. A. Vydrov, G. E. Scuseria, L. A. Constantin, X. Zhou, and K. Burke, "Erratum: Restoring the Density-gradient Expansion for Exchange in Solids and Surfaces (Physical Review Letters (2008) 100 (136406))," Phys. Rev. Lett. **102**, 39902 (2009).

[33]J. Padilla and D. Vanderbilt, "Ab initio study of $BaTiO_3$ surfaces," Phys. Rev. B **56**, 1625–1631 (1997).

[34]Y. Yang, F. Gao, S. Gao, and S.-H. Wei, "Origin of the stability of two-dimensional perovskites: a first-principles study," Journal of Materials Chemistry A **6**, 14949–14955 (2018).

[35]J.-M. Zhang, F. Ma, K.-W. Xu, and X.-T. Xin, "Anisotropy analysis of the surface energy of diamond cubic crystals," Surface and Interface Analysis **35**, 805–809 (2003).

[36]Z. Ning, X. Gong, R. Comin, G. Walters, F. Fan, O. Voznyy, E. Yassitepe, A. Buin, S. Hoogland, and E. H. Sargent, "Quantum-dot-in-perovskite Solids," Nature **523**, 324–328 (2015).

[37]T. Chen, B. J. Foley, C. Park, C. M. Brown, L. W. Harriger, J. Lee, J. Ruff, M. Yoon, J. J. Choi, and S.-H. Lee, "Entropy-driven structural transition and kinetic trapping in formamidinium lead iodide perovskite," Sci. Adv. **2**, e1601650–e1601650 (2016).

[38]D. Yang, J. Lv, X. Zhao, Q. Xu, Y. Fu, Y. Zhan, A. Zunger, and L. Zhang, "Functionality-Directed Screening of Pb-Free Hybrid Organic–Inorganic Perovskites with Desired Intrinsic Photovoltaic Functionalities," Chemistry of Materials **29**, 524–538 (2017).

[39]D. Gammon, E. S. Snow, B. V. Shanabrook, D. S. Katzer, and D. Park, "Fine Structure Splitting in the Optical Spectra of Single GaAs Quantum Dots," Phys. Rev. Lett. **76**, 3005–3008 (1996).

[40]J. Even, L. Pedesseau, and C. Katan, "Understanding Quantum Confinement of Charge Carriers in Layered 2d Hybrid Perovskites," Chem. Phys. Chem. **15**, 3733–3741 (2014).

[41]A. N. Beecher, O. E. Semonin, J. M. Skelton, J. M. Frost, M. W. Terban, H. Zhai, A. Alatas, J. S. Owen, A. Walsh, and S. J. L. Billinge, "Direct Observation of Dynamic Symmetry Breaking above Room Temperature in Methylammonium Lead Iodide Perovskite," ACS Energy Lett. **1**, 880–887 (2016).

[42]O. Yaffe, Y. Guo, L. Z. Tan, D. A. Egger, T. Hull, C. C. Stoumpos, F. Zheng, T. F. Heinz, L. Kronik, M. G. Kanatzidis, J. S. Owen, A. M. Rappe, M. A. Pimenta, and L. E. Brus, "Local Polar Fluctuations in Lead Halide Perovskite Crystals," Phys. Rev. Lett. **118**, 136001 (2017).

[43]J. Even, m. Carignano, and C. Katan, "Molecular disorder and translation/rotation coupling in the plastic crystal phase of hybrid perovskites," Nanoscale (2015).

[44]A. M. A. Leguy, A. R. Goñi, J. M. Frost, J. Skelton, F. Brivio, X. Rodríguez-Martínez, O. J. Weber, A. Pallipurath, M. I. Alonso, M. Campoy-Quiles, M. T. Weller, J. Nelson, A. Walsh, and P. R. F. Barnes, "Dynamic disorder, phonon lifetimes, and the assignment of modes to the vibrational spectra of methylammonium lead halide perovskites," Phys. Chem. Chem. Phys. **18**, 27051–27066 (2016).

[45]A. Poglitsch and D. Weber, "Dynamic disorder in methylammoniumtrihalogenoplumbates (II) observed by millimeter-wave spectroscopy," J. Chem. Phys. **87**, 6373–6378 (1987).

[46]R. X. Yang, J. M. Skelton, E. L. da Silva, J. M. Frost, and A. Walsh, "Spontaneous Octahedral Tilting in the Cubic Inorganic Caesium Halide Perovskites $CsSnX_3$ and CsPbX3 (X = F, Cl, Br, I)," J. Phys. Chem. Lett. **8**, 4720–4726 (2017).

[47]M. A. Becker, R. Vaxenburg, G. Nedelcu, P. C. Sercel, A. Shabaev, M. J. Mehl, J. G. Michopoulos, S. G. Lambrakos, N. Bernstein, J. L. Lyons, T. Stöferle, R. F. Mahrt, M. V. Kovalenko, D. J. Norris, G. Rainò, and A. L. Efros, "Bright triplet excitons in caesium lead halide perovskites," Nature **553**, 189–193 (2018).

[48]A. Miyata, A. Mitioglu, P. Plochocka, O. Portugall, J. T.-W. Wang, S. D. Stranks, H. J. Snaith, and R. J. Nicholas, "Direct measurement of the exciton binding energy and effective masses for charge carriers in organic–inorganic tri-halide perovskites," Nat. Phys. **11**, 582–587 (2015).

[49]K. Zheng, Q. Zhu, M. Abdellah, M. E. Messing, W. Zhang, A. Generalov, Y. Niu, L. Ribaud, S. E. Canton, and T. Pullerits, "Exciton Binding Energy and the Nature of Emissive States in Organometal Halide Perovskites," J. Phys. Chem. Lett. **6**, 2969–2975 (2015).

[50]S. Rana, K. Awasthi, S. S. Bhosale, E. W.-G. Diau, and N. Ohta, "Temperature-Dependent Electroabsorption and Electrophotoluminescence and Exciton Binding Energy in $MAPbBr_3$ Perovskite Quantum Dots," J. Phys. Chem. C **123**, 19927–19937 (2019).

α-phase

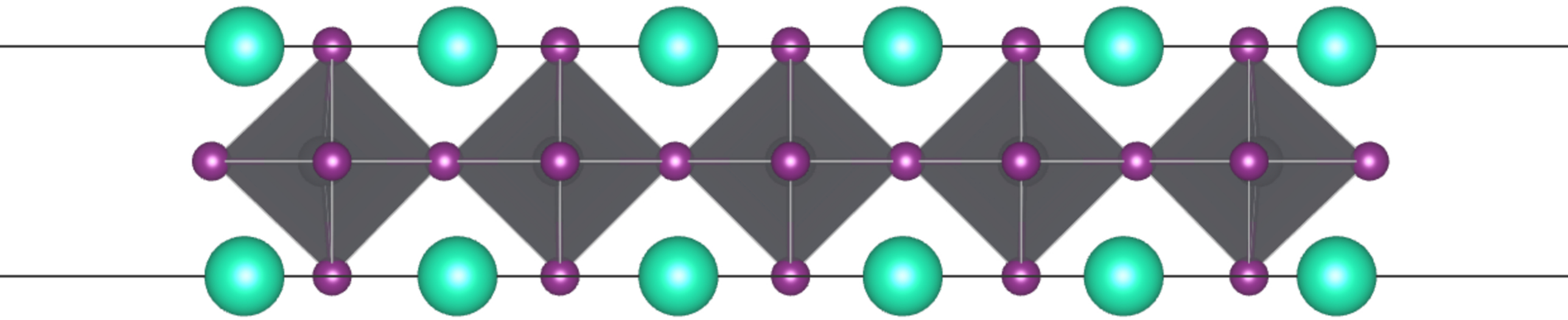

γ-phase

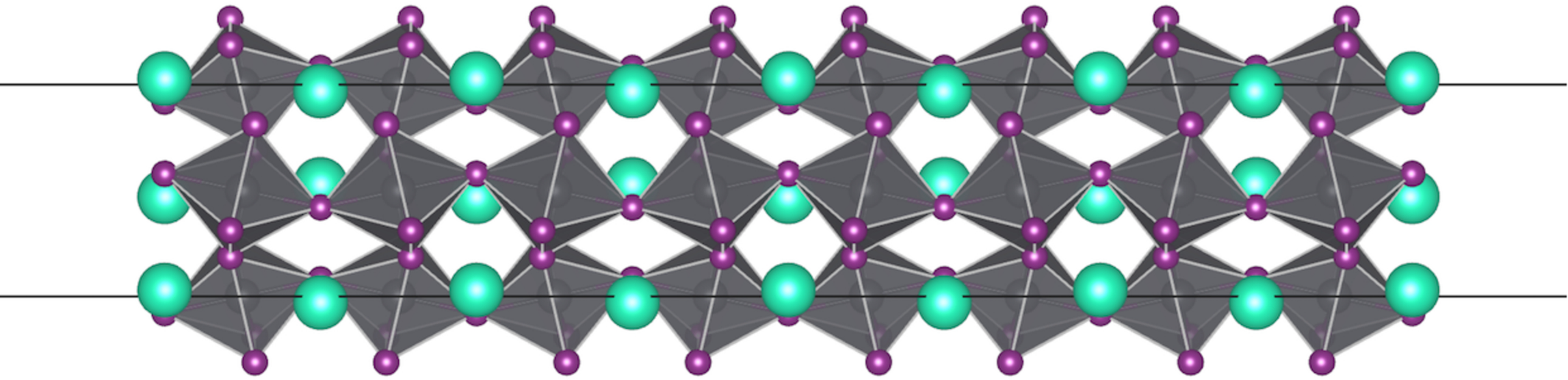

δ-phase

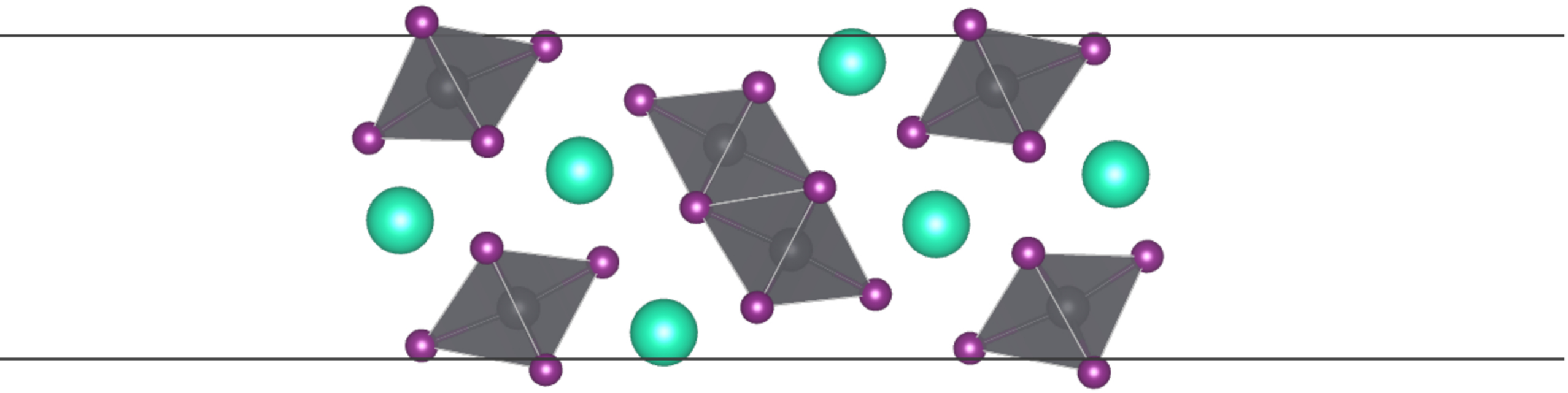

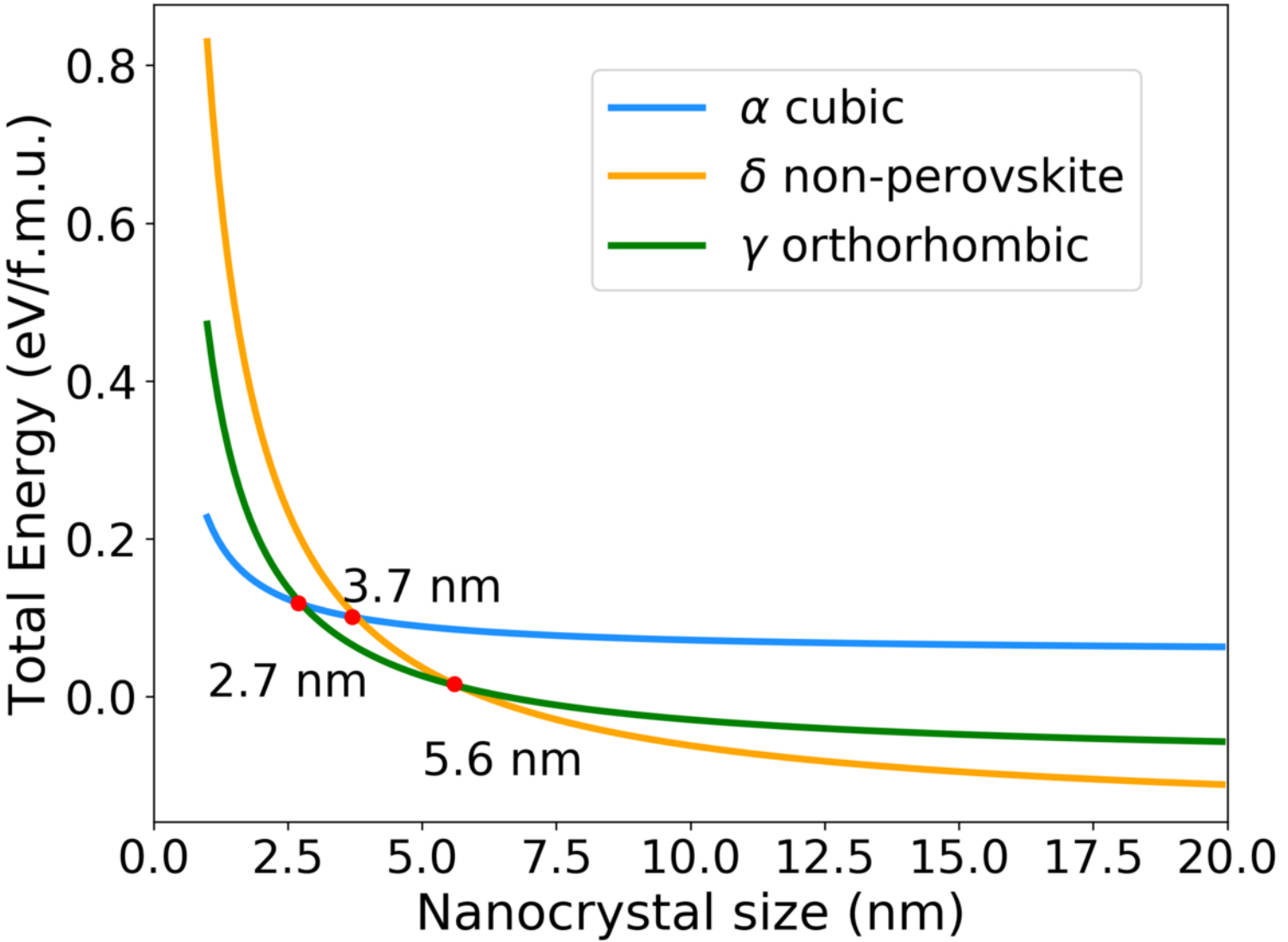
α cubic
δ non-perovskite
γ orthorhombic
3.7 nm
2.7 nm
5.6 nm
Total Energy (eV/f.m.u.)
Nanocrystal size (nm)
0.8
0.6
0.4
0.2
0.0
0.0
2.5
5.0
7.5
10.0
12.5
15.0
17.5
20.0

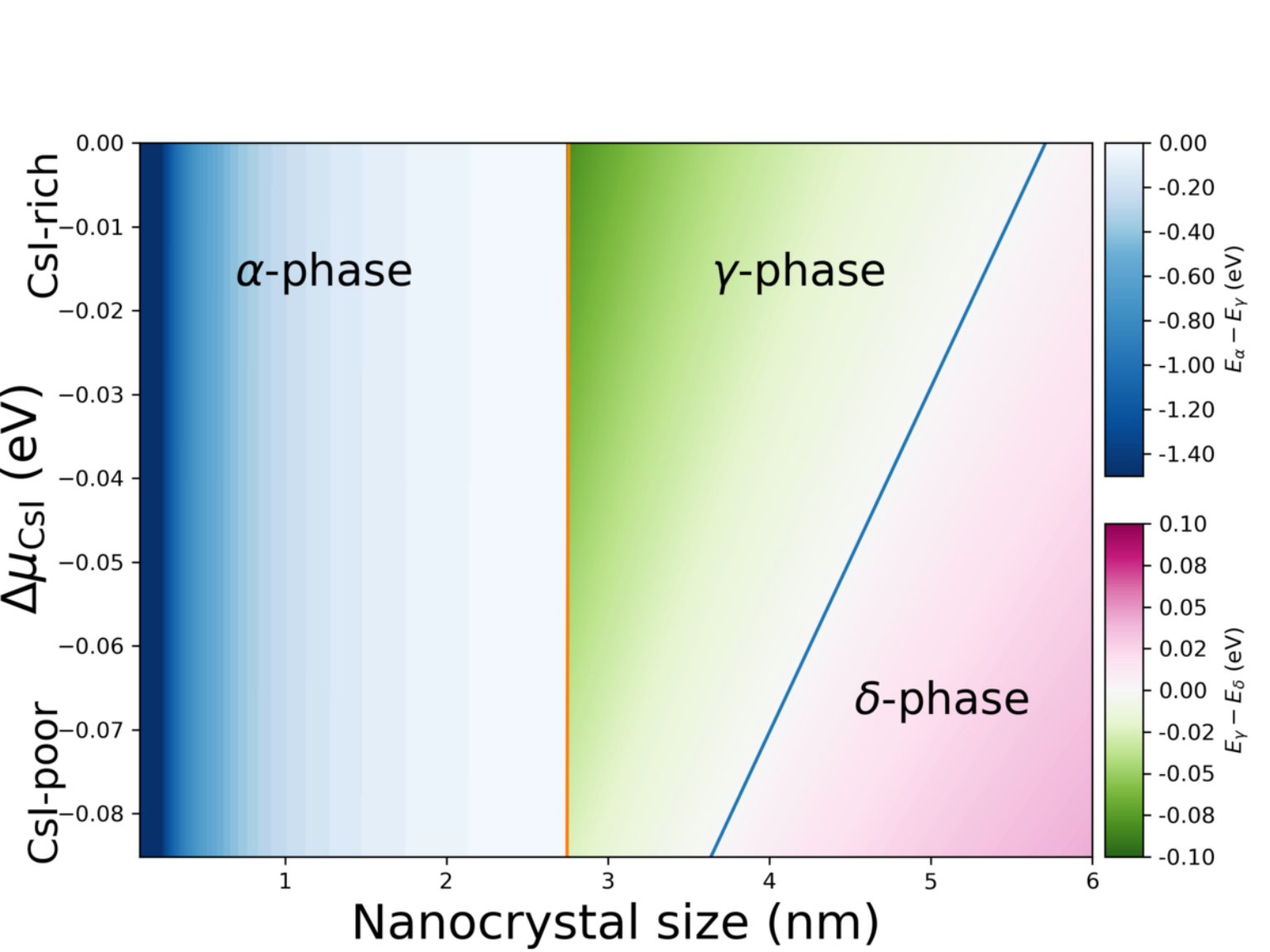
α-phase
γ-phase
δ-phase
CsI-rich
CsI-poor
$\Delta\mu_{CsI}$ (eV)
0.00
−0.01
−0.02
−0.03
−0.04
−0.05
−0.06
−0.07
−0.08
1
2
3
4
5
6
Nanocrystal size (nm)
$E_\alpha - E_\gamma$ (eV)
0.00
-0.20
-0.40
-0.60
-0.80
-1.00
-1.20
-1.40
$E_\gamma - E_\delta$ (eV)
0.10
0.08
0.05
0.02
0.00
-0.02
-0.05
-0.08
-0.10

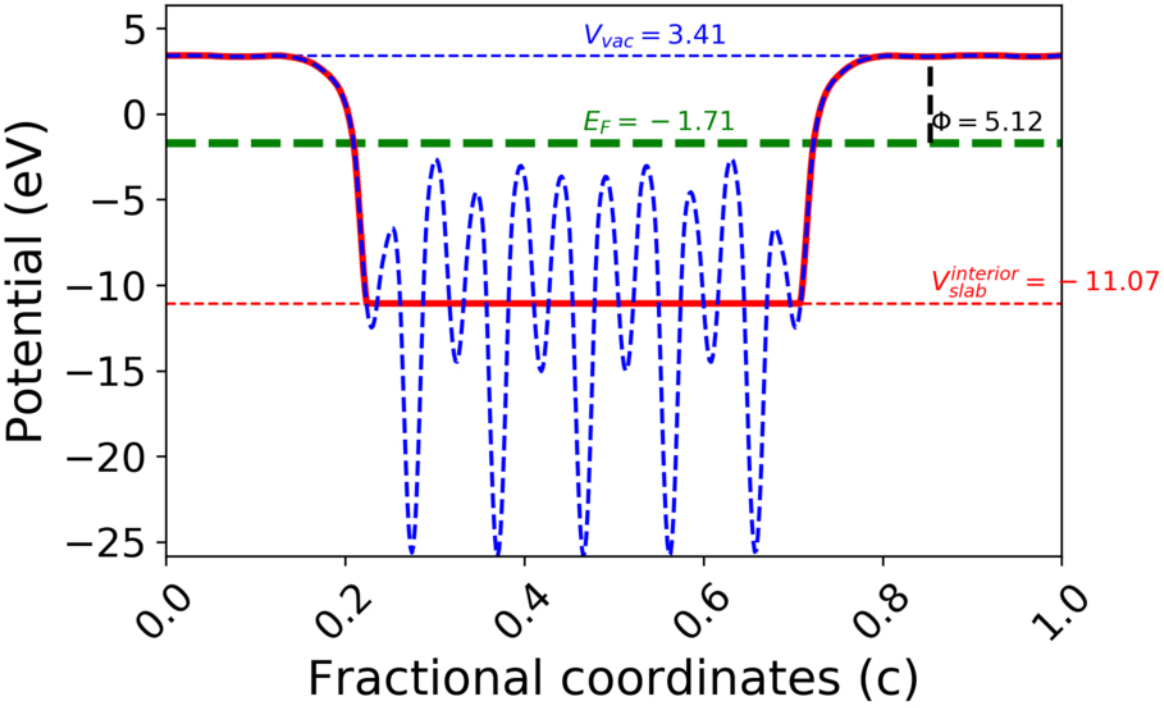
$V_{vac} = 3.41$
$E_F = -1.71$
$\Phi = 5.12$
$V_{slab}^{interior} = -11.07$
Potential (eV)
Fractional coordinates (c)
5
0
−5
−10
−15
−20
−25
0.0
0.2
0.4
0.6
0.8
1.0

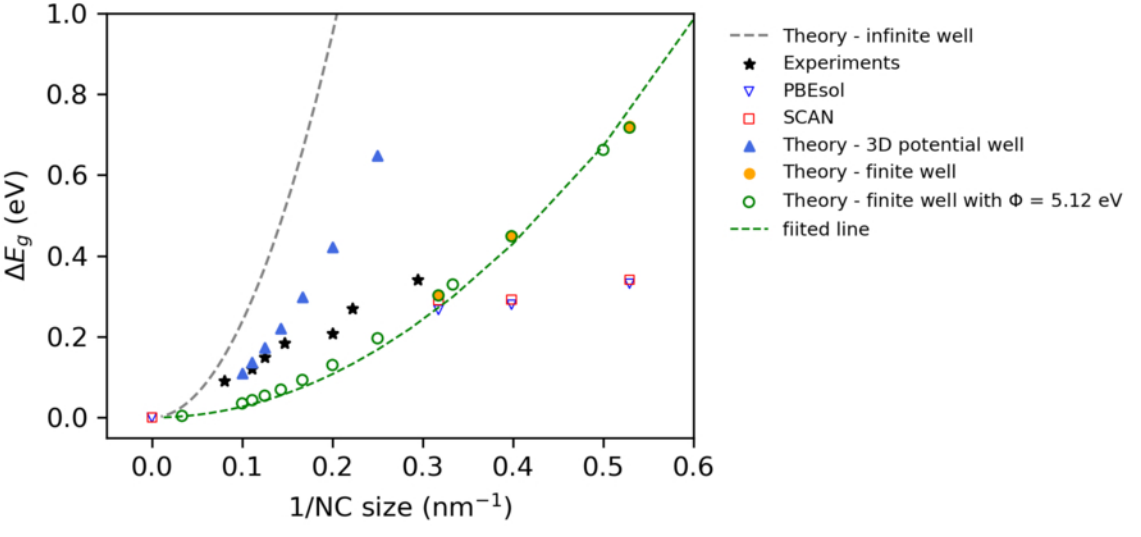
1.0
0.8
0.6
0.4
0.2
0.0
ΔE_g (eV)
0.0
0.1
0.2
0.3
0.4
0.5
0.6
1/NC size (nm^{-1})
Theory - infinite well
Experiments
PBEsol
SCAN
Theory - 3D potential well
Theory - finite well
Theory - finite well with Φ = 5.12 eV
fiited line